Helical magnetism in Sr-doped $CaMn_7O_{12}$ films

Amanda Huon[1], Anuradha M. Vibhakar[2], Alexander J. Grutter[3], Julie A. Borchers[3], Steven Disseler[3], Yaohua Liu[4], Wei Tian[4], Fabio Orlandi[5], Pascal Manuel[5], Dmitry D. Khalyavin[5], Yogesh Sharma[6], Andreas Herklotz[6], Ho Nyung Lee[6], Michael R. Fitzsimmons[4,7], Roger D. Johnson[2], and Steven J. May[1]*

[1]Department of Materials Science and Engineering, Drexel University, Philadelphia, PA 19104, USA

[2]Clarendon Laboratory, Department of Physics, University of Oxford, Oxford, OX1 3PU, UK

[3]NIST Center for Neutron Research, National Institute of Standards and Technology, Gaithersburg, Maryland 20899, USA

[4]Neutron Scattering Division, Oak Ridge National Laboratory, Oak Ridge, TN 37831, USA

[5]ISIS Facility, Rutherford Appleton Laboratory, Chilton, Didcot, Oxon, OX11 0QX, United Kingdom

[6]Materials Science and Technology Division, Oak Ridge National Laboratory, Oak Ridge, TN 37831, USA

[7]Department of Physics and Astronomy, University of Tennessee, Knoxville, TN 37996, USA

*E-mail: smay@drexel.edu

Abstract

Noncollinear magnetism can play an important role in multiferroic materials but is relatively understudied in oxide heterostructures compared to their bulk counterparts. Using variable temperature magnetometry and neutron diffraction, we demonstrate the presence of helical magnetic ordering in $CaMn_7O_{12}$ and $Ca_{1-x}Sr_xMn_7O_{12}$ (for x up to 0.51) thin films. Consistent with bulk $Ca_{1-x}Sr_xMn_7O_{12}$, the net magnetization increases with Sr doping. Neutron diffraction confirms that the helical magnetic structure remains incommensurate at all values of x, while the fundamental magnetic wavevector increases upon Sr substitution. This result demonstrates a chemical-based approach for tuning helical magnetism in quadruple perovskite films and enables future studies of strain and interfacial effects on helimagnetism in oxide heterostructures.

I. INTRODUCTION

In magnetic oxide films, a variety of features can be employed such as epitaxial strain, interfacial electronic/orbital reconstructions, dimensionality, and local structural coupling that give rise to ordered spin orientations that are distinct from their bulk counterparts [1,2]. While much work has focused on ferromagnetic and antiferromagnetic systems, non-collinear magnetic structures, such as periodic spin helices, in oxide heterostructures remains relatively unexplored. There is growing interest in noncollinear magnetic states stabilized by spin orbit coupling, local inversion symmetry breaking, and/or competing exchange energies, such as helices and skyrmions, which may enable new multiferroics or low-power spintronics [3]. The majority of recent progress in noncollinear spin textures has come in the form of metallic films, with far fewer studies of helical magnetism within oxide heterostructures [4-6]. Having been recently synthesized in thin film form, the quadruple perovskite $CaMn_7O_{12}$ is a potential system for studying the effects of biaxial strain, finite thickness, and interfacial coupling - scientific directions only accessible in thin films - on noncollinear magnetism in oxide heterostructures. However, the magnetic properties of epitaxial $CaMn_7O_{12}$ films have yet to be reported.

This quadruple perovskite manganite has garnered growing attention in recent years due to complex physics and numerous ordered states, making it a material of interest for multiferroic behavior [7-20]. Bulk $CaMn_7O_{12}$ exhibits four distinct phase transitions: a commensurate charge-ordering and structural transition [8,21], an orbital ordering transition [14,22,23], a simultaneous helical magnetic/ferroelectric transition (T_{N1}) and a second magnetic transition that modifies the helical magnetic state (T_{N2}) [9,12,13]. $CaMn_7O_{12}$ is a quadruple perovskite with the $AA'_3B_4O_{12}$ stoichiometry, such that the A-sites are occupied by Ca^{2+} ions and the A'- and B-sites are occupied by Mn ions. The A'-site Mn cations have a nominal oxidation state of 3+ at all

temperatures and the *B*-site Mn ions have a nominal valence of 3.25+ in the high temperature phase. The high temperature (> 440 K) structure of $CaMn_7O_{12}$ is cubic, space group $Im\bar{3}$, with a lattice parameter of 7.38162(1) Å [24]. Below ~440 K, the compound undergoes concurrent structural and electronic transitions, resulting in charge-ordering of the *B*-site Mn ions with a 3:1 occupation of Mn^{3+} and Mn^{4+}, respectively, as evidenced by powder diffraction [8,21]. The unit cell contracts along the body diagonal and the crystal structure becomes rhombohedral (space group $R\bar{3}$) with lattice parameters of $a_h = b_h = 10.45891(2)$ Å, $c_h = 6.34262(1)$ Å and interaxial lattice angles of $\alpha = 90°$, $\beta = 90°$ and $\gamma = 120°$ in the hexagonal setting [24]. Below ~250 K, $CaMn_7O_{12}$ orbitally orders with an incommensurate propagation vector k_s of length $|Q| \approx 2.06$ Å^{-1} (defined outside of the first Brillouin zone), parallel to the hexagonal *c*-axis or equivalently to the pseudocubic (pc) $[111]_{pc}$ direction, which corresponds to the alternating occupation of the $d_{3x^2-r^2}$ and the $d_{3y^2-r^2}$ electronic orbitals on the *B*-site Mn^{3+} ions [14]. In addition to the charge and orbital ordering transitions, $CaMn_7O_{12}$ also magnetically orders in an incommensurate helical structure at 90 K (T_{N1}), with a propagation vector k_0 of length $|Q| \approx 1.03$ Å^{-1} also parallel to the $[111]_{pc}$ direction, which induces an electric polarization aligned parallel to k_0. In this phase, the coupling between the orbital and magnetic orders is commensurate, such that $k_s = 2k_0$. This magneto-orbital coupling also gives rise to a $3k_0$ component of the magnetic helix, which describes a higher order modulation in the helicity, i.e. due to the orbital order there exist periodic changes to the spin angles between adjacent Mn-containing planes. Below 48 K (T_{N2}), $CaMn_7O_{12}$ undergoes a second magnetic phase transition at which the orbital and magnetic propagation vectors become unlocked, but the modulation of the magnetic helicity persists via incommensurate magneto-orbital coupling, resulting in a series of additional magnetic diffraction peaks corresponding to Fourier components of the modulated helix [18].

In this paper, we focus on understanding the nature of the magnetic ground state in $Ca_{1-x}Sr_xMn_7O_{12}$ thin films probed using neutron diffraction and magnetometry. Although the ordered magnetic structure was previously determined for $CaMn_7O_{12}$ and $SrMn_7O_{12}$ by neutron diffraction [25], and magnetometry from lightly doped ($x < 0.2$) polycrystalline $Ca_{1-x}Sr_xMn_7O_{12}$ has been measured [26], detailed magnetic characterization of quaternary $Ca_{1-x}Sr_xMn_7O_{12}$ has not been reported, and questions remain related to thin films of these materials. Do thin films of quadruple perovskites also exhibit helical magnetism and how are the magnetic properties altered due to the chemical pressure with isoelectronic Sr doping? Even in strain-relaxed films, it is not clear *a priori* if a modulated spin helix will persist unperturbed, due to the presence of the film/substrate interface, defects that arises from strain relaxation, and the increased importance of the surface compared to bulk crystals. For example, the spin structure of $BiFeO_3$ has been shown to differ from bulk materials in strain-relaxed films.[5,6,27,28] We previously reported the electronic properties of $Ca_{1-x}Sr_xMn_7O_{12}$ thin films and found that the charge-ordering transition can be tuned by 40 K in Sr-alloyed solid solution films with $x = 0.6$ [29]. Here we show that the films exhibit a very similar helical ground state as bulk $CaMn_7O_{12}$ and that the substitution of Sr leads to a systematic increase in the helical magnetic wavevector. As Sr and Ca are isovalent, the change in magnetic behavior is ascribed to the Sr-induced lattice expansion.

II. EXPERIMENTAL TECHNIQUES

$Ca_{1-x}Sr_xMn_7O_{12}$ thin films were synthesized using oxide molecular beam epitaxy (MBE) followed by *ex situ* post-growth anneal to fully oxidize the films. The films, ranging from 100 to 130 nm in thickness, were deposited on 1x1 cm^2 $SrLaAlO_4$ (SLAO) (001) substrates. Our recent papers report on the growth conditions and transport data of similar $Ca_{1-x}Sr_xMn_7O_{12}$ films [29,30], although those reported in Ref. 29 were deposited on $(La,Sr)(Al,Ta)O_3$ (LSAT) substrates. The

films for the present study were synthesized at a growth temperature of 650°C and pressure of $2x10^{-6}$ mmHg in O_2. Following growth, the samples were oxidized *ex situ* in a tube furnace using a two-step anneal: first heating them at 850°C with flowing O_2 for 3 hours, then cooled to 200°C for 1 hour under an ozone atmosphere (95:5) O_2:O_3 mixture to achieve oxidized films [29,30].

Each sample was characterized by X-ray diffraction (XRD), Raman spectroscopy, superconducting quantum interference device (SQUID) magnetometery, and neutron diffraction measurements. The cation stoichiometry [Mn:(Ca+Sr) ratio] was determined by Rutherford backscattering spectrometry (RBS) on films grown on MgO (001) substrates that were positioned directly adjacent to films grown on SLAO substrates. XRD was carried out using a four-circle high resolution X-ray diffractometer (X'Pert Pro, Panalytical) [31] (Cu Kα_1 radiation) at room temperature. Reciprocal space maps (RSMs) of the 103_{pc} film peaks were measured to determine the in-plane lattice parameter. Additionally, a Rigaku SmartLab diffractometer [31], fitted with a Cu X-ray source, was used to analyze rhombohedral domains of the $CaMn_7O_{12}$ thin film. A Renishaw 1000 confocal Raman microscope was used to measure Raman spectra in back scattering configuration [31]. Each spectrum is a sum average of 10 individual spectra taken at different places on the sample through a 20× objective. The wavelength of the Raman laser used in these measurements was 532 nm. Magnetization measurements were carried out using a SQUID magnetometer (Quantum Design, MPMS3) [31], for which the Sr-containing samples and one of the ternary $CaMn_7O_{12}$ films were cleaved into 5x5 mm^2 samples after the neutron diffraction data were collected. The magnetization as a function of temperature (*M* vs *T*) curves were measured after field-cooling with a field of $\mu_0 H$ = 0.1 T. The temperature-dependent magnetization data were collected at a rate of 6 K/minute and recorded from 10 K to 300 K using sweep mode. Magnetization as a function of field (*M* vs *H*) was measured after zero field cooling

to 10 K. Neutron diffraction measurements were performed at four beamlines: WISH at the ISIS Neutron and Muon Source, CORELLI at the Spallation Neutron Source, and the SPINS and BT-7 instruments at the NIST Center for Neutron Research (NCNR). Polarized neutron beam experiments were performed on the BT-7 triple-axis spectrometer at the NCNR. For the polarization measurements the neutron energy (14.7 meV) was selected with a pyrolitic graphite monochromator and analyzer, and pyrolitic graphite filters were utilized to remove contamination from higher-order wavelengths. Polarization of the neutron beam was achieved with two ^{3}He neutron spin filters in mumetal shielded solenoids positioned before and after the sample [32]. The spin state of the incident and scattered neutrons (up ↑ or down ↓) was chosen using *in situ* NMR, resulting in polarization efficiencies exceeding 97%.

We note that throughout the manuscript, we use a pseudocubic notation in which directions in real and reciprocal space are defined within the simple cubic perovskite unit cell, such that the pseudocubic 111 is equivalent to the 003 of the $CaMn_7O_{12}$ rhombohedral lattice in the hexagonal setting. **Table S1** gives the relevant reciprocal lattice directions in the pseudocubic, quadruple perovskite cubic, and quadruple perovskite hexagonal settings. The transformation matrices to convert between all three bases are given by equations 1-6 in the Supplementary Material.

III. RESULTS AND DISCUSSION

A. Structure

The out-of-plane 2θ-θ XRD patterns in **Figure 1(a)** show only 00l reflections from the film confirming that the films are phase pure with a [001] growth direction. The peak shifts with increasing Sr concentration are consistent with a Sr-induced lattice expansion previously observed in $Ca_{1-x}Sr_xMn_7O_{12}$ films grown on (001)-oriented LSAT [29]. A similar lattice

expansion is observed in bulk $SrMn_7O_{12}$ compared to $CaMn_7O_{12}$ [25,26,34-36]. **Figure 1(b)** shows the reciprocal space maps around the 103 peak of the $Ca_{1-x}Sr_xMn_7O_{12}$ films. For all films, the Q_x peak positions are slightly shifted to larger momentum transfer values than the SLAO substrates. This observation demonstrates that the $Ca_{1-x}Sr_xMn_7O_{12}$ films are not constrained to match the in-plane lattice of the substrates and are instead strain relaxed due to the lattice mismatch of approximately ≈ 1.8% ($CaMn_7O_{12}$ a_{pc} ≈ 3.682 Å, SLAO a_{pc} ≈ 3.75 Å). To confirm the structural symmetry in our $Ca_{1-x}Sr_xMn_7O_{12}$/SLAO heterostructures, micro-Raman spectroscopy measurements were performed at room temperature. According to group theory analysis, rhombohedral $CaMn_7O_{12}$ with $R\bar{3}$ space group, shows 12 Raman active modes ($6A_g$ + $6E_g$) [37]. **Figure 1(c)** shows the room temperature Raman spectra of the $Ca_{1-x}Sr_xMn_7O_{12}$ films with different Sr-doping concentrations. The observed phonon modes were assigned in accordance with the reported results on single crystals of $CaMn_7O_{12}$ [22,37,38] and $Ca_{1-x}Sr_xMn_7O_{12}$ [39]. Based on the symmetry assignment, Raman spectra in **Figure 1(c)** confirmed the presence of six phonon modes of E_g and three phonon modes of A_g symmetry, consistent with the preservation of rhombohedral crystal symmetry in the $Ca_{1-x}Sr_xMn_7O_{12}$ thin films. We have also observed an additional mode at 670 cm^{-1}, indicated by the solid gray line in **Figure 1(c)**, in agreement with the reported results on single crystals of $CaMn_7O_{12}$, however the reason of appearance of this new Raman mode is not understood yet [22]. The measured Raman modes are presented in **Table S2** in the Supplemental Material [33].

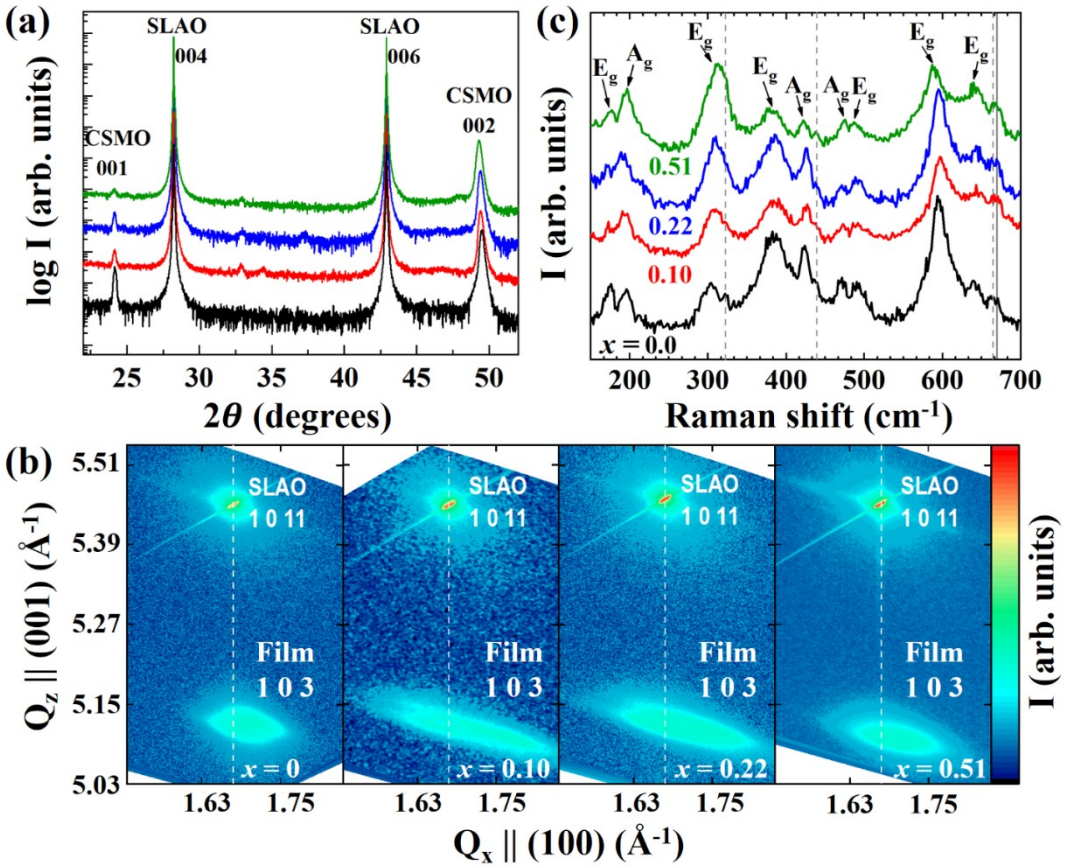

FIG. 1. Effect of Sr doping on the crystal structure of $Ca_{1-x}Sr_xMn_7O_{12}$ films synthesized on $SrLaAlO_4$. (a) 2θ-θ x-ray diffraction scans of $Ca_{1-x}Sr_xMn_7O_{12}$ films displaying the 00*l* reflections of the pseudocubic structure. The *c*-axis expands with increasing Sr doping. The data sets are presented in order of Sr content with the x = 0 data on bottom (black line) and the x = 0.51 data on top (green line). (b) RSMs show the 103 Bragg reflection of $Ca_{1-x}Sr_xMn_7O_{12}$ films, confirming that the in-plane strain is relaxed. (c) Room temperature Raman spectra of the $Ca_{1-x}Sr_xMn_7O_{12}$ films exhibits nine active modes. The Raman modes of the substrate are indicated by the dotted lines.

Below the cubic to rhombohedral phase transition one might expect the formation of four rhombohedral domains as observed in single crystal of $CaMn_7O_{12}$ [40]. Accordingly, the epitaxial growth of $Ca_{1-x}Sr_xMn_7O_{12}$ on (001) SLAO substrates allows the formation of four rhombohedral domains given the four-fold symmetry of the (001) tetragonal substrate. The four

domains correspond to the rhombohedral distortion of the cubic unit cell along each of the four body diagonals. Consider the {111} family of pseudo-cubic reflections parallel to the body diagonals. In the true rhombohedral symmetry this family is split, giving a unique [111] direction along which the unit cell is contracted, and a sub-family of $\bar{1}11$, $1\bar{1}1$ and $\bar{1}\bar{1}1$reflections that remain symmetry equivalent. If all four domains are present, then one would expect two experimental signatures in the XRD data. Firstly, the 111 reflections of each rhombohedral domain will be measured at the same value of 2θ, but at four different orientations of the film related by the same four-fold symmetry that interchanges the domains. Secondly, in the vicinity of a given 111 reflection, there will occur additional diffraction intensity from the $\bar{1}11$, $1\bar{1}1$ and $\bar{1}\bar{1}1$ reflections of the other three domains, respectively. The domain fractions can then be quantified by comparing the relative intensities of the four reflections measured at all four positions. In the following characterization of a $CaMn_7O_{12}$ film we choose to study the {222} family as opposed to the {111} family, as they afford us a more convenient scattering geometry. However, the above arguments still apply. The film was first aligned so that the 222 reflection of a given domain was in the scattering condition, which is inclined at ~35° from the surface of the film. A line scan through a RSM taken at this reflection, **Figure 2(d)** and **2(e)**, shows an asymmetric peak shape indicative of two separate reflections that are not fully resolved. In **Figure 2(e)** the smaller peak at larger |Q| corresponds to that of the 222 reflection and the larger peak at smaller |Q| corresponds to the $\bar{2}22, 2\bar{2}2, \wedge\bar{2}\bar{2}2$reflections. The angular separation between the two peaks was fitted to be 0.94(1)°, which is 0.1° smaller than that calculated using the bulk lattice parameters reported in reference [35]. Hence the rhombohedral distortion observed from the films is smaller than that of the $CaMn_7O_{12}$ single crystals. Furthermore, the relative intensity of the two peaks was determined to be of the 1:3 ratio. The analysis was

repeated for a series of 90° rotations about the surface normal and returned the same 1:3 ratio, thus, the film is composed of equal populations of all four domains. Furthermore, the film was checked for reverse rhombohedral twins, but only obverse rhombohedral reflections were observed.

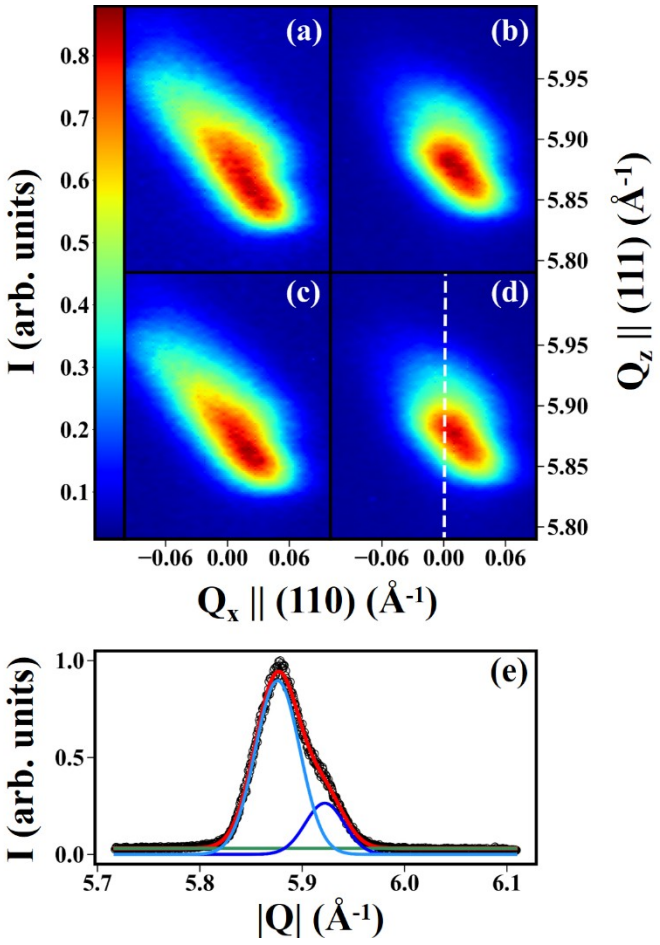

FIG. 2. (a) – (d) Normalized reciprocal space maps about the 222 reflection for each of the four rhombohedral domains within the undoped $CaMn_7O_{12}$ film. (e) Fitted line scan taken through (d). The raw data is given by the black circles, the total fitted data by the red line, the polynomial background by the green line and the two diffraction peaks by the blue lines.

B. Magnetic Properties

Temperature dependent magnetometry was performed to determine how the change of lattice volume induced by Sr-doping alters the magnetization and magnetic transition temperatures. In **Fig. 3(a),** the magnetization (M) measurements with an applied field of $\mu_0 H$ = 0.1 T clearly show the second magnetic phase transition in this series of films at $T_{N2} \sim 50$ K, and an enhancement in the ground state magnetic susceptibility is observed upon increasing the Sr-doping concentration. The T_{N2} value is found to increase from 48 K, for ternary $CaMn_7O_{12}$, to approximately 58 K for the $x = 0.51$ sample, as determined by linear extrapolation of M as a function of temperature. Furthermore, a subtle change in the temperature dependence of M near ~90 K is present, which suggests a magnetic transition at T_{N1}. **Figure 3(b)** shows M vs. H data for the series of samples at 10 K. The $Ca_{1-x}Sr_xMn_7O_{12}$ films display similar hysteresis loops with weak ferromagnetic-like behavior and a trend of M_s increasing with increasing Sr concentration. The saturation magnetization values are small, suggesting that the magnetization arises from canted moments; however, it is also possible that rhombohedral domain boundaries, the surface, or film/substrate interface effects also contribute to the magnetization. These results are consistent with bulk $CaMn_7O_{12}$ and $SrMn_7O_{12}$, where T_{N2} has been reported near 48 K and 63 K in the respective compounds [25] and have shown enhancement of the net magnetization under applied magnetic fields by increasing the Sr-doping [26].

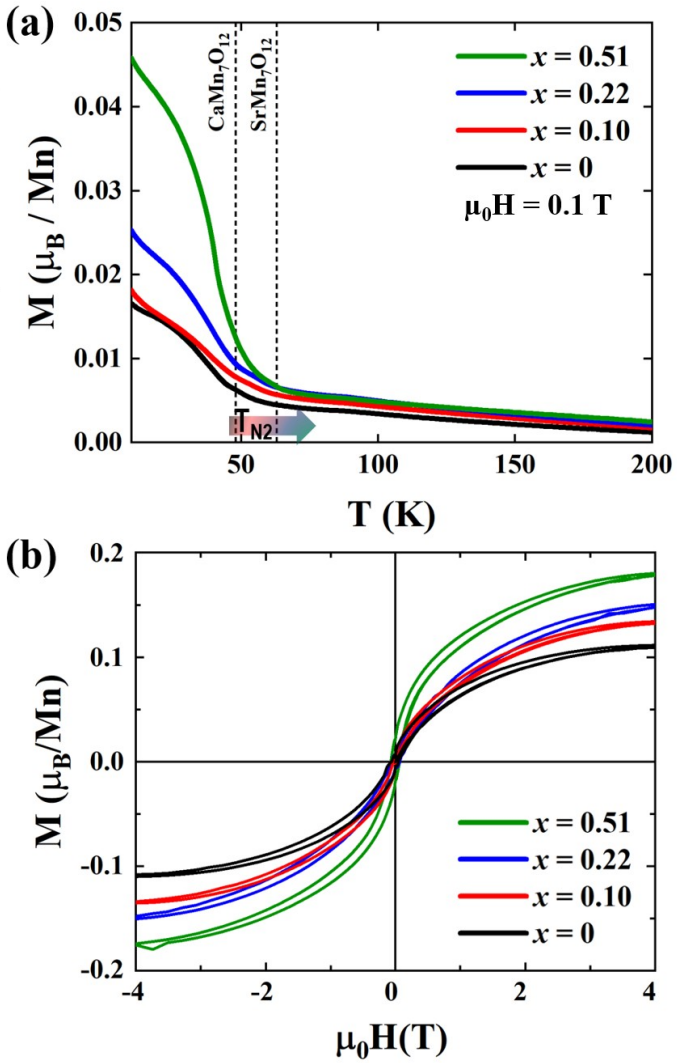

FIG. 3. (a) Temperature dependence of magnetization measured with $\mu_0 H$ = 0.1 T applied parallel to the film surface of the $Ca_{1-x}Sr_xMn_7O_{12}$ films. Magnetization data in (a) were obtained upon warming after field-cooling in 0.1 T. The vertical dotted lines show the T_{N2} values reported for bulk $CaMn_7O_{12}$ and $SrMn_7O_{12}$ in Ref. [25], for comparison. (b) Magnetization as a function of applied field at 10 K.

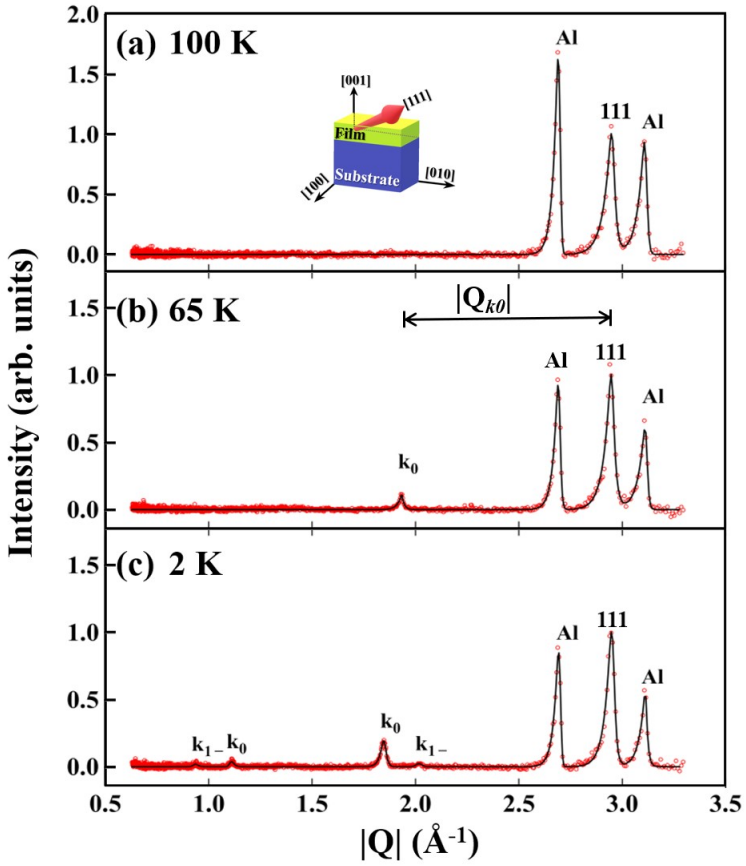

FIG. 4. Neutron diffraction data along the pseudocubic [111] direction obtained from the $CaMn_7O_{12}$ film using the WISH instrument at sample temperatures of 100 K, 65 K, and 2 K. The raw data minus the background are given by the red circles and the fitted peaks are given by the solid black line. The magnetic satellite peaks are labelled as in [18]. The inset of (a) shows a schematic of the scattering vector with respect to the thin film geometry, while $|Q_{k0}|$ is defined in (b).

Neutron diffraction was used to confirm the presence of helical magnetic ordering in the $Ca_{1-x}Sr_xMn_7O_{12}$ thin films. We begin by presenting data on the parent compound, $CaMn_7O_{12}$ thin film. We note that the implication of four rhombohedral domains in these films is that only ~1/4 of the film contributes to the scattered intensity of a given magnetic peak, and thus all magnetic intensities are relatively weak compared with structural Bragg peaks that have unresolved contributions from all four rhombohedral domains. Importantly, the magnetic propagation

vectors can be uniquely identified in the presence of domains. **Figure 4** shows the neutron diffraction data measured on the $CaMn_7O_{12}$ film at temperatures of 2 K, 65 K, and 100 K along the [111] direction. Three temperature-independent reflections were observed above $|Q| = 2.5$ Å^{-1}; two of these reflections come from the Al sample mount and the third is that of the 111 $CaMn_7O_{12}$ nuclear peak. At 100 K, no magnetic satellite peaks were observed, consistent with the paramagnetic phase of $CaMn_7O_{12}$. At 65 K ($T_{N2} < T < T_{N1}$), a single magnetic reflection was measured at $|Q| = 1.93(1)$ Å^{-1}, corresponding to the magnetic satellite at $k_{111} - k_0$ arising from the incommensurate helical magnetic order [18]. We denote the length of the k_0 wavevector in Å^{-1} as $|Q_{k0}|$, as shown in Fig. 4(b); the length of k_0 in reciprocal lattice units is 1.12 with respect to the *c*-axis of the hexagonal unit cell as described in the Supplemental Material. Below T_{N2} at 2 K, four magnetic peaks are present, corresponding to two k_0 and two k_{1-} satellite reflections, as labelled in **Figure 4(c)** and defined by $k_{1-} = k_s - k_0$. With increasing $|Q|$, the first four reflections in Figure 4(c) correspond to k_{1-}, k_0, $k_{111} - k_0$ and $k_{111} - k_{1-}$. The satellite k_{1-} peaks arise from the higher order modulation of the magnetic helicity. The presence of these satellite peaks therefore is also indicative of the presence of orbital order within the films, similar to bulk. Following the same analysis from Ref. 18, the measured magnetic and nuclear peaks can be modeled to obtain the hexagonal *c*-axis parameter, the magnetic wavevector (k_0), and the orbital ordering wavevector (k_s) in both magnetically ordered phases. The calculated values are in good agreement with bulk single crystals, as detailed in supplemental **Table S3**.

We have also performed polarized neutron diffraction measurements from the $CaMn_7O_{12}$ film at the BT-7 triple-axis diffractometer at a base temperature of 3 K. The neutron beam polarization was first aligned parallel to the scattering vector of the k_0 peak at $|Q| \approx 1.85$ Å^{-1}, and all four spin cross sections were measured. In this configuration [41,42], the non-spin flip

scattering (↑↑ and ↓↓) is structural in origin and the spin flip scattering (↑↓and ↓↑) is magnetic. The non-spin flip scattering is negligible, confirming that the k_0 is entirely magnetic with no structural contribution, as expected. The neutron polarization was next aligned perpendicular to the scattering vector to isolate the vector components of the moments. In this configuration in the absence of structural scattering [41,42], the non-spin flip scattering originates from the magnetization parallel to the neutron beam polarization axis, and the spin-flip scattering comes from the magnetization perpendicular to both the polarization axis and the scattering vector Q. As shown in **Figure S3**, the intensities of the spin-flip and non-spin-flip peaks are approximately equal, indicating that the magnetization components parallel and perpendicular to the polarization axis are equal as expected a helical spin structure.

Having established the presence of helical ordering within the $CaMn_7O_{12}$ film, we next turn to the influence of Sr substitution. In the following, the k_0 magnetic peak near $|Q| \approx 1.85$ Å^{-1} was also measured using neutron diffraction from the series of films with x ranging from 0 to 0.51. **Figure 5** presents neutron diffraction data measured on the SPINS triple-axis diffractometer from the undoped $CaMn_7O_{12}$ ($x = 0$) and Sr-doped ($x = 0.22$) films. The diffraction temperature maps in **Figure 5(a)** show that below the magnetic transition temperatures, a clear peak is observed that corresponds to the k_0 peak at $|Q| \approx 1.85$ Å^{-1} in Figure 4. Similar results are obtained from the $x = 0.22$ sample, as shown in **Figure 5(b)**, albeit with a slight shift in the |Q| vector from ≈1.852 Å^{-1} to ≈1.841 Å^{-1} for $x = 0$ and $x = 0.22$, respectively, at low temperatures. Furthermore, on warming the $x = 0.22$ sample from low temperatures, the intensity of the magnetic reflection decreases and the position of the magnetic peak moves toward larger |Q| until T_{N2} (~50 K). The magnetic peak for this sample does not move its position from 50 K to 60 K.

Above 90 K, the magnetic peak is no longer present. Similar trends were observed in data collected from the $x = 0.51$ sample, as shown in **Figures S2** in Supplemental Materials.

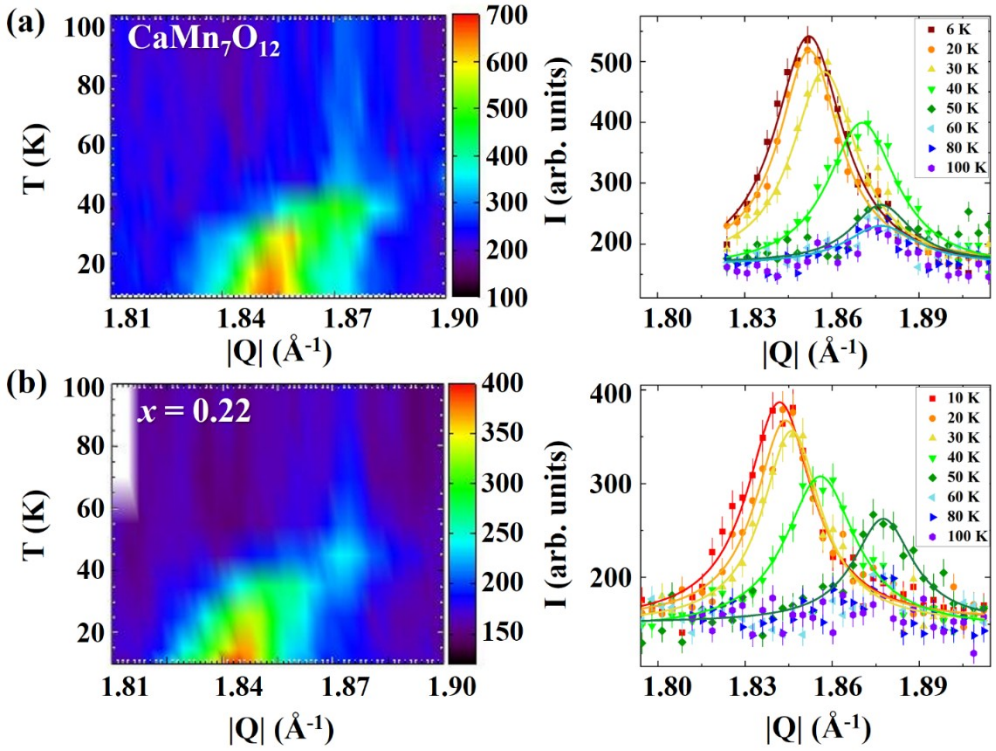

FIG. 5. Neutron diffraction temperature maps for (a) $CaMn_7O_{12}$ and (b) $Ca_{0.78}Sr_{0.22}Mn_7O_{12}$. Adjacent plots to the right show the intensity as a function of |Q| at individual temperatures. In all plots, the |Q| vector is along the [111] direction. Error bars indicate square root of number of counts.

Figure 6(a) shows $|Q_{k0}|$ plotted as a function of temperature for three compositions. All three compositions exhibit an abrupt shift of $|Q_{k0}|$ to larger values as the temperature is decreased below ~50 K, consistent with a second magnetic transition at T_{N2}. The effect of Sr substitution can be seen in **Figure 6(b)** in which the length of the fundamental magnetic propagation vector, k_0, at low temperatures (2 – 10 K) is plotted as a function of Sr concentration. We find that increasing Sr concentration shifts the length of this vector to larger values, which is consistent to the trend from Ca/Sr parent end members in bulk [25]. The length of k_0 ranges from ≈ 1.12 Å^{-1} ($x = 0.51$) to ≈ 1.108 Å^{-1} ($x = 0$), revealing an increase of ≈ 1 %. Note that for the data represented

by closed symbols in **Figure 6(b)**, $|Q_{k0}|$ was calculated using the low temperature k_0 position and the room temperature pseudocubic lattice parameters. This may lead to a slight underestimation of $|Q_{k0}|$.

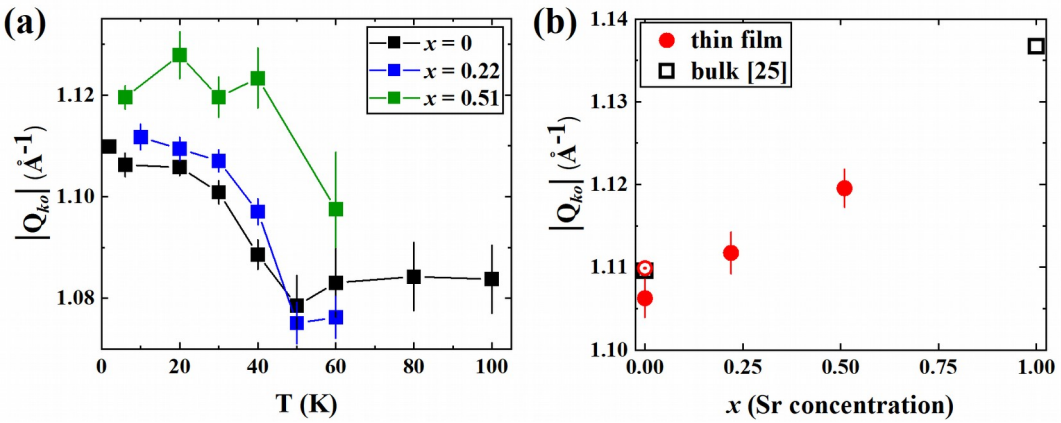

FIG. 6. The length of the k_0 wavevector as a function of (a) temperature and (b) Sr concentration at the lowest temperatures measured. The two x = 0 data points were obtained at 2 K with the WISH diffractometer (open circle) and 6 K with the SPINS instrument (closed circle) from different $CaMn_7O_{12}$ samples. The x = 0.51 sample was measured at 6 K and the x = 0.22 sample was measured at 10 K. Data from bulk $CaMn_7O_{12}$ and $SrMn_7O_{12}$ measured at 1.5 K is represented by open squares; this data comes from Ref. 25. Error bars represent ±1 standard deviation.

These results provide insight into how the magnetic ordering evolves upon *A*-site substitution between the $CaMn_7O_{12}$ and $SrMn_7O_{12}$ parent compounds. While it was previously known that the k_0 vector is ~3% larger in $SrMn_7O_{12}$ than in $CaMn_7O_{12}$ [25], the data shown in **Fig. 6(b)** demonstrates that the magnetic wavevector smoothly expands as x is increased in $Ca_{1-x}Sr_xMn_7O_{12}$. The increase in wavevector indicates that the Sr-induced lattice expansion modifies the exchange interactions by either increasing the Mn-O bond lengths or the Mn-O-Mn bond

angles, both of which are known to directly alter exchange energies in ferromagnetic and antiferromagnetic perovskite manganites [43,44]. Previous theoretical work on $CaMn_7O_{12}$ has revealed seven exchange pathways that contribute to the helical state [15-17]. Thus, identifying which interactions are most sensitive to the lattice expansion is beyond the scope of this experimental study and warrants future theoretical investigation. Additionally, *A*-site cation disorder, present in the quaternary alloys due to the random site substitutions of Ca and Sr, does not suppress the magnetic transition temperatures or alter the magnetic structure. We note that in quaternary perovskite manganites, *A*-site disorder and cation size variance can significantly decrease ordering temperatures [45]. Our results suggest that quadruple manganites may be more robust against cation disorder, and thus follow Vegard behavior when alloyed, because the non-transition metal cations (here alkaline earth Sr or Ca) occupy only 1/8 of the total cation sites instead of 1/2 of the cation sites in conventional perovskite manganite.

The confirmation of modulated helical magnetism in quadruple manganite films opens the door to future studies of how strain, thickness, and superlattice formation can be used to alter or control helimagnetism in oxide heterostructures. For example, superlattices of $CaMn_7O_{12}/SrMn_7O_{12}$ could prove an interesting system for exploring how magnetic ordering is perturbed at heterohelical interfaces. Further, the ability to probe complex modulated magnetic structures via neutron diffraction in epitaxial quadruple perovskites should enable new measurements within this family of materials as many such compounds are not yet available as bulk single crystals.

IV. CONCLUSION

We show how substituting Sr into $CaMn_7O_{12}$ films affects the magnetic properties by magnetometry and neutron diffraction. The substitution of Sr for Ca in $Ca_{1-x}Sr_xMn_7O_{12}$ leads to a

linear lattice expansion with increasing Sr concentration as expected based on the ionic radii of Ca and Sr. This structural expansion results in an enhanced saturation magnetization and an increase in T_{N2} by ~10 K at the $x = 0.51$ composition compared to the $x = 0$ parent compound. Neutron diffraction measurements confirmed the presence of helical magnetic order in all the $Ca_{1-x}Sr_xMn_7O_{12}$ films with $x = 0$ to 0.51, where for all samples the length of the fundamental magnetic propagation vector, k_0, was found to be approximately 1.08 $Å^{-1}$ in the first magnetically ordered phase ($T_{N2} < T < T_{N1}$). As observed in bulk single crystals, higher order Fourier components of the magnetic structure were observed below T_{N2} (~50 K) in the $CaMn_7O_{12}$ film. These additional peaks are consistent with a modulation of the helicity of the magnetic structure along its propagation vector due to incommensurate magneto-orbital coupling. With increasing Sr content to $x = 0.51$, the period of the magnetic helix decreases by ~1%. The ability to tune the magnetic helix through Sr/Ca substitutions in quadruple perovskite films should enable future studies of the relationship between electric polarization and the helical spin structure, as well as interfacial helical magnetic coupling in $CaMn_7O_{12}$-related heterostructures.

ACKNOWLEDGEMENTS

A. H. was supported by the U.S. Department of Energy (DOE), Office of Science, Office of Workforce Development for Teachers and Scientists, Office of Science Graduate Student Research (SCGSR) program. The SCGSR program is administered by the Oak Ridge Institute for Science and Education for the DOE under contract number DE-SC0014664. S. J. M. was supported by the Army Research Office (W911NF-15-1-0133); A. H. also acknowledges partial support from W911NF-15-1-0133. R. D. J. acknowledges support from a Royal Society University Research Fellowship. The authors thank W. Chen, R. Erwin, L. Harriger, Md. T.

Hassan, S. Watson, Z. Xu, and Y. Zhao for supporting the 3He and neutron diffraction measurements at the NCNR. The work at ORNL was supported by U.S. DOE, Office of Science, Basic Energy Sciences, Materials Science and Engineering Division (XRD and SQUID characterizations). This work also used resources of Spallation Neutron Source and High Flux Isotope Reactor, which are DOE Office of Science User Facilities. The authors acknowledge the Science and Technology Facility Council (STFC, UK) for the provision of neutron beam time on the WISH instrument.

REFERENCES

1. A. Bhattacharya and S. J. May, Annu. Rev. Mater. Res. **44**, 65 (2014).
2. Y. Liu and X. Ke, J. Phys.: Condens. Matter **27**, 373003 (2015).
3 F. Hellman, et al., Rev. Mod. Phys. **89**, 025006 (2017).
4. S. Chavraverty, T. Matsuda, H. Wadati, J. Okamoto, Y. Yamasaki, H. Nakao, Y. Murakami, S. Ishiwata, M. Kawasaki, Y. Taguchi, Y. Tokura, and H. Y. Hwang, Phys. Rev. B **88**, 220405(R) (2013).
5. W. Ratcliff, D. Kan, W. Chen, S. Watson, S. Chi, R. Erwin, G. J. McIntyre, S. C. Capelli, and I. Takeuchi, Adv. Funct. Mater. **21**, 1567 (2011).
6. X. Ke, P. P. Zhang, S. H. Baek, J. Zarestky, W. Tian, and C. B. Eom, Phys. Rev. B **82**, 134448 (2010).
7. B. Bochu, J. Chenavas, J. C. Joubert, and M. Marezio, J. Solid State Chem. **11**, 88 (1974).
8. I. O. Troyanchuk, L. S. Lobanovsky, N. V. Kasper, M. Hervieu, A. Maignan, and C. Michel, Phys. Rev. B **58**, 14903 (1998).
9. R. Przenioslo, I. Sosnowska, D. Hohlwein, T. Hauβ, I. O. Troyanchuk, Solid State Commun. **111**, 687 (1999).
10. R. Przeniosło, I. Sosnowska, E. Suard, A. Hewat, and A. N. Fitch, J. Phys.: Condens. Matter **14**, 5747 (2002).
11. A. N. Vasil'ev and O. S. Volkova, Low Temp. Phys. **33**, 895 (2007)
12. G. Zhang, S. Dong, Z. Yan, Y. Guo, Q. Zhang, S. Yunoki, E. Dagotto, and J.-M. Liu, Phys. Rev. B **84**, 174413 (2011).
13. R. D. Johnson, L. C. Chapon, D. D. Khalyavin, P. Manuel, P. G. Radaelli, and C. Martin, Phys. Rev. Lett. 108, 067201 (2012).
14. N. J. Perks, R. D. Johnson, C. Martin, L. C. Chapon, P. G. Radaelli, Nature Commun. **3**, 1277 (2012).
15. X. Z. Lu, M.-H. Whangbo, S. Dong, X. G. Gong, and H. J. Xiang, Phys. Rev. Lett. **108**, 187204 (2012).

16. J. T. Zhang, X. M. Lu, J. Zhou, H. Sun, F. Z. Huang, and J. S. Zhu, Phys. Rev B **87**, 075127 (2013).
17. K. Cao, R. D. Johnson, N. Perks, F. Giustino, and P. G. Radaelli, Phys. Rev. B **91**, 064422 (2015).
18. R. D. Johnson, D. D. Khalyavin, P. Manuel, A. Bombardi, C. Martin, L. C. Chapon, and P. G. Radaelli, Phys. Rev. B **93**, 180403(R) (2016).
19. N. Terada, Y. S. Glazkova, and A. A. Belik, Phys. Rev. B **93**, 155127 (2016).
20. J. S. Lim, D. Saldana-Greco, and A. M. Rappe, Phys. Rev. B **97**, 045115 (2018).
21. W. Sławiński, R. Przeniosło, I. Sosnowska, M. Bieringer, I. Margiolaki, A. N. Fitch and E. Suard, J. Phys.: Condens. Matter **20**, 104239 (2008).
22. X. Du, R. Yuan, L. Duan, C. Wang, Y. Hu, Y. Li, Phys. Rev. B **90**, 104414 (2014).
23. S. M. Souliou, Y. Li, X. Du, M. Le Tacon, and A. Bosak, Phys. Rev. B **94**, 184309 (2016).
24. A. A. Belik, Y. S. Glazkova, Y. Katsuya, M. Tanaka, A. V. Sobolev, and I. A. Presniakov., J. Phys. Chem. C **120**, 8278 (2016).
25. R. D. Johnson, D. D. Khalyavin, P. Manuel, P. G. Radaelli, I. S. Glazkova, N. Terada, and A. A. Belik, Phys. Rev. B **96**, 054448 (2017).
26. H-G. Zhang, X-C. Ma, and L. Xie, International Journal of Modern Physics B **29**, 1550221 (2015).
27. H. Beá, M. Bibes, X.-H. Zhu, S. Fusil, K. Bouzehouane, S. Petit, J. Kreisel, and A. Barthélémy, Appl. Phys. Lett. **93**, 072901 (2008).
28. W. Saenrang, B. A. Davidson, F. Maccherozzi, J. P. Podkaminer, J. Irwin, R. D. Johnson, J. W. Freeland, J. Íñiguez, J. L. Schad, K. Reierson, J. C. Frederick, C. A. F. Vaz, L. Howard, T. H. Kim, S. Ryu, M.v. Vennendaal, P. G. Radaelli, S. S. Dhesi, M. S. Rzchowski, and C. B. Eom, Nature Commun. **8**, 1583 (2017).
29. A. Huon, D. Lee, A. Herklotz, M. R. Fitzsimmons, H. N. Lee and S. J. May, APL Mater. **5**, 096105 (2017).
30. A. Huon, A. C. Lang, D. Saldana-Greco, J. S. Lim, E. J. Moon, A. M. Rappe, M. L. Taheri, and S. J. May, Appl. Phys. Lett. **107**, 142901 (2015).
31. Any mention of commercial products is for information only; it does not imply recommendation or endorsement by NIST.
32. W. C. Chen, G. Armstrong, Y. Chen, B. Collett, R. Erwin, T. R. Gentile, G. L. Jones, J. W. Lynn, S. McKenney, and J. E. Steinberg, Physica B **397**, 168 (2007)
33. See Supplemental Material at [] for crystallographic transformation matrices and for additional Raman spectra, neutron diffraction data, and analysis of diffraction data.
34. Y. S. Glazkova, N. Terada, Y. Matsushita, Y. Katsuya, M. Tanaka, A. V. Sobolev, I. A. Presniakov, and A. A. Belik, Inorg. Chem. **54**, 9081 (2015).
35. A. A. Belik, Y. S. Glazkova, Y. Katsuya, M. Tanaka, A. V. Sobolev, and I. A. Presniakov., J. Phys. Chem. C **120**, 8278 (2016).
36. H. M. Liu, S. Dong, Z. Z. Du, P. Chu and J.-M. Liu, EPL **108**, 67012 (2014).
37. M. N. Iliev, V. G. Hadjiev, M. M. Gospodinov, R. P. Nikolova, and M. V. Abrashev, Phys. Rev B **89**, 214302 (2014).
38. A. Nonato, B. S. Araujo, A. P. Ayala, A. P. Maciel, S. Yanez-Vilar, M. Sanchez-Andujar, M. A. Senaris-Rodriguez, and C. W. A. Paschoal, Appl. Phys. Lett. **105**, 222902 (2014).
39. P. Jain, J. Saha, L.C. Gupta, S. Patnaik, A.K. Ganguli, and R. Chatterjee, AIP Adv. **7**, 055832 (2017).

40. R. Yuan, L. Duan, X. Du, and Y. Li, Phys. Rev. B **91**, 054102 (2015).
41. R. M. Moon, T. Riste, and W. C. Koehler, Phys. Rev. **181**, 920 (1969).
42. S. Seki, Y. Yamasaki, M. Soda, M. Matsuura, K. Hirota, and Y. Tokura, Phys. Rev. Lett. **100**, 127201 (2008).
43. P. G. Radaelli, G. Iannone, M. Marezio, H. Y. Hwang, S.-W. Cheong, J. D. Jorgensen, and D. N. Argyriou, Phys. Rev. B **56**, 8265 (1997).
44. O. Chmaissem, B. Dabrowski, S. Kolesnik, J. Mais, D. E. Brown, R. Kruk, P. Prior, B. Pyles, and J. D. Jorgensen, Phys. Rev. B **64**, 134412 (2001).
45. L. M. Rodriguez-Martinez and J. P. Attfield, Phys. Rev. B **54**, R15622 (1996).